Three-Dimensional Collagen Topology Shapes Cell Morphology, beyond Stiffness

Changchong Chen, Zeinab Ibrahim, Marion Marchand, Tristan Piolot, Sahil Kamboj, Franck Carreiras, Ayako Yamada, Marie-Claire Schanne-Klein, Yong Chen, Ambroise Lambert, et al.

3D collagen topology shapes cell morphology, beyond stiffness

Changchong Chen,[§] Zeinab Ibrahim,[§] Marion F. Marchand,[±] Tristan Piolot,[±] Sahil Kamboj,[#] Franck Carreiras,[#] Ayako Yamada,[§] Marie-Claire Schanne-Klein,[¦] Yong Chen,[§] Ambroise Lambert[#] and Carole Aimé*[§]*

[§] PASTEUR, Département de chimie, École normale supérieure, PSL University, Sorbonne Université, CNRS, 24 rue Lhomond, 75005 Paris, France

[±] Center for Interdisciplinary Research in Biology (CIRB), Collège de France, CNRS, INSERM, PSL Research University, 11 place Marcelin Berthelot, Paris, France

[#] Equipe de Recherche sur les Relations Matrice Extracellulaire-Cellules, ERRMECe, (EA1391), Groupe Matrice Extracellulaire et physiopathologie (MECuP), Institut des Matériaux, I-MAT (FD4122), CY Cergy Paris Université, Maison Internationale de la Recherche, Rue Descartes, 95031 Neuville sur Oise Cedex, France.

[¦] Laboratoire d'Optique et Biosciences (LOB), École polytechnique, CNRS, Inserm, Institut Polytechnique de Paris, Route de Saclay, 91128 Palaiseau cedex, France

***** Corresponding authors: ambroise.lambert@u-cergy.fr; carole.aime@ens.psl.eu

KEYWORDS. Extracellular matrix, *in vitro* models, collagen topology, cellular heterogeneity, second harmonic generation.

ABSTRACT. Cellular heterogeneity is associated with many physiological processes, including pathological ones, such as morphogenesis and tumorigenesis. The extracellular matrix (ECM) is a key player in the generation of cellular heterogeneity. Advances in our understanding rely on our ability to provide relevant *in vitro* models. This requires to catch the characteristics of the tissues that are essential for controlling cell fate. To do this, we must consider the diversity of tissues, the diversity of physiological contexts, and the constant remodeling of ECM along these processes. To this aim, we have fabricated a library of ECM models for reproducing the scaffold of connective tissues and basement membrane by using different biofabrication routes based on the electrospining and drop casting of biopolymers from the ECM. Using a combination of electron microscopy, multiphoton imaging and AFM nanoindentation, we show that we can vary independently protein composition, topology and stiffness of ECM models. This in turns allows to generate the *in vivo* complexity of the phenotypic landscape of ovarian cancer cells. We show that, while this phenotypic shift cannot be directly correlated with a unique ECM feature, the 3D collagen fibril topology patterns cell shape, beyond protein composition and stiffness of the ECM. On this line, this work is a further step towards the development of ECM models recapitulating the constantly remodeled environment that cells face, and thus provides new insights for cancer model engineering and drug testing.

1. INTRODUCTION

The extracellular matrix (ECM) plays a central role in the generation of cellular heterogeneity, being the scene of extensive transformations in diverse pathophysiological contextes.[1-10] Recent works have shed light on the importance of cell interactions with ECM components in cancer[11,12] and during embryogenesis[13] underscoring the regulation from both mechanical and biochemical stimuli.[14-17] Indeed, because cellular heterogeneity is central to tumor metastasis and has been correlated with chemoresistance,[1] understanding its triggers is a significant challenge from a fundamental and therapeutic perspective. Yet, one of the largest hurdles to the better understanding of cellular heterogeneity is the establishment of models that recapitulate the complexity of the 3D microenvironment and its constant remodeling during tumor progression. In particular, providing *in vitro* models with only ECM proteins remains an important challenge with a particular emphasis on the possibility to vary the architecture without affecting mechanical properties.[18] To this aim, original approaches have recently emerged making use of macromolecular crowding to tune collagen fibril topology without significantly altering matrix stiffness.[19,20] Tissue engineering strategies are another way of controlling the architecture of biomimetic matrices by directly impacting the topology of collagen fibrils. As such, they are useful tools for understanding how the ECM can trigger cellular heterogenity.

As cellular model, we use SKOV-3 human ovarian adenocarcinoma cells because they display a large cellular heterogeneity.[21-24] Indeed, ovarian cancers are very sensitive to their surrounding microenvironment. This includes the soluble environment - the ascite - which is an excess fluid in physio-pathological conditions,[25] but also the biochemical and mechanical features of the ECM. Important morphological changes, in terms of composition and topology have been reported in human normal and malignant *ex vivo* ovarian biopsies using advanced multiphoton imaging combining second harmonic generation (SHG) with 2-photon excited fluorescence (2PEF).[26,27] To

address this combinatorial challenge, we use porous supports, called patches (Fig.1), to host ECM models while independently varying ECM composition, topology, and stiffness. (1) We use only proteins from the ECM. First, type I collagen is used to mimic the scaffold of connective tissues as it is the primary ECM component of most solid tumors and influences metastatic progression, and by far the major structural element of the ovarian stroma. Second, laminin and type IV collagen are used to mimic the basement membrane (BM). BM remodeling in pre-malignant ovarian surface epithelium has been shown to mostly impact these two proteins with transient loss.[28-30] Note that fibronectin also plays a key role in ovarian cancer, notably as circulating component of the ascitic malignant fluid. Nevertheless, the complexity of the biological context led us to select a limited number of ECM features and defer the study of fibronectin to future work focusing on the circulating environment. (2) We vary the topology of the ECM models playing with the processing of type I collagen. Our strategy to tune collagen fibril architecture uses electrospinning (**es**) and dropcasting (**dc**) (Fig.1). (3) We can vary the stiffness of the ECM models independently from the composition and topology by varying the dimension of the patch (Fig.1B and Fig.2A). Very importantly, for all investigated ECM models, we reach a physiological (including pathological) stiffness, which is a crucial prerequisite for such studies.

In a first step, we have used a combination of scanning electron microscopy (SEM), multiphoton microscopy (SHG and 2PEF) and atomic force microscopy (AFM) to characterize the topology and mechanical properties of the ECM models. We have then explored the generated cellular heterogeneity in SKOV-3 cells depending on the features of the ECM models. Measurement of cell heterogeneity is crucial but remains difficult to quantify because of the existence of a continuum of phenotypic variations that cannot be carefully distinguished by biochemical bulk assays. To tackle this limit, we have combined qualitative immuno-fluorescence observations with

a morphological single cell profiling quantification.[31] We have focused on the variation of the nucleus structure, which is among the most important morphological changes observed in tumor cells.[32-34] Indeed, quantitative analysis of cancer cell nuclear morphology has been used in cancer diagnosis. Here we have measured that the cellular heterogeneity generated by the diverse ECM models is represented by two nuclear shape modes: the size and shape. These morphological variations have a complex, not straightforward dependency on the features of the ECM models, supporting that either protein composition, topology or stiffness can be dominant for determining cell population.[35] Our strategy is a straightforward tool for providing ECM microenvironments where one parameter can prevail over the other, while preserving biological relevance in the meantime. Very importantly, it provides a way to decorrelate connective tissue topology from protein composition and matrix stiffness. As such, this work will have a great impact for improving the engineering of cancer models, helping identify therapies for better patient outcomes.

2. MATERIALS AND METHODS

2.1. Type I collagen extraction and purification. Type I collagen was extracted and purified from rat tail tendons as previously described, except that we used 3 mM hydrochloric acid instead of 500 mM acetic acid.[36,37] Collagen purity was assessed by electrophoresis and its concentration estimated by hydroxyproline titration.[38] All other chemicals were purchased and used as received. Water was purified with a Direct-Q system (Millipore Co.).

2.2. Patch fabrication. Patches similar to the ones that are commercially available from the Mesobiotech® company were fabricated by photolithography and soft-lithography in the lab (see Supporting Information). These patches were coated with gold by sputter deposition for

electrospinning (route A, Fig.1) or for improving hydrophilicity and drop casting (route B, Fig.1). For this, we used an Emitech K675X Sputter Coater System working at 125 mA for 30 seconds.

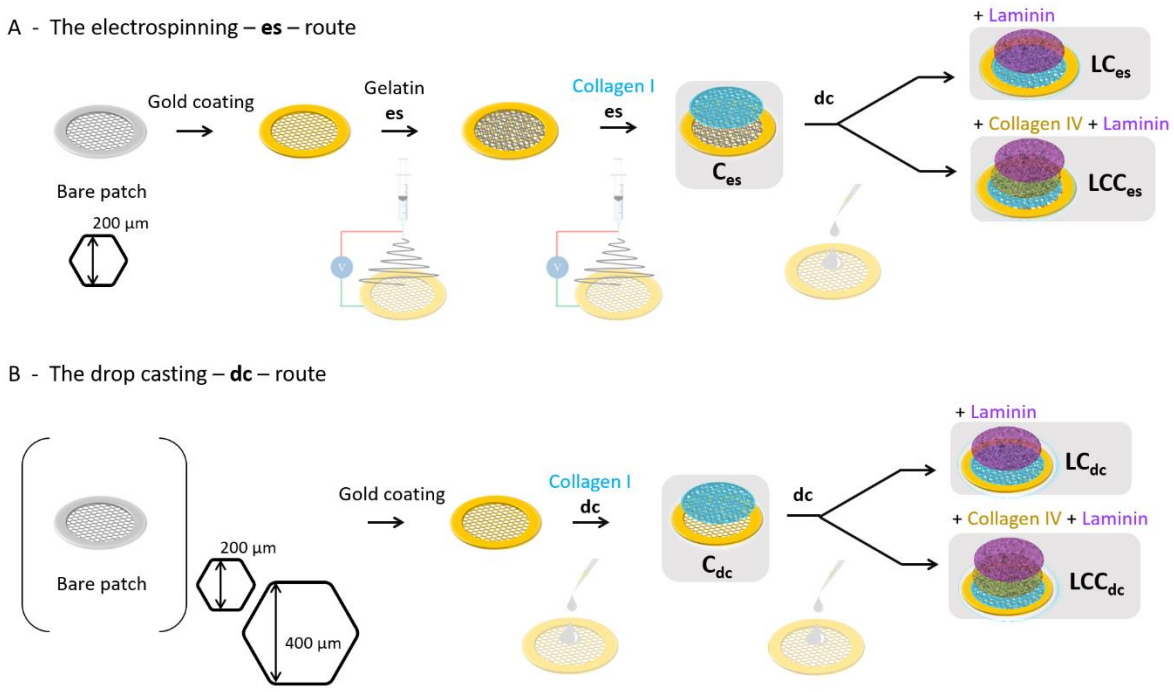

Figure 1. Scheme of the preparation of the ECM models based on (A) electrospinning (**es**) and (B) drop casting (**dc**) of ECM proteins including collagen I, collagen IV and laminin.

2.3 Electrospinning (es). The gelatin solution was prepared by dissolving 100 mg of gelatin in a mixture of 420 µL acetic acid, 280 µL ethyl acetate and 200 µL DI water. Citric acid (10 mg) was then added as thermal cross-linking agent before **es**. The mixture was stirred for 4 hours at room temperature. Gelatin was electrospun onto a gold-coated patch fixed on a tin foil (7 cm in diameter) at a voltage of 11 kV for 7 minutes at a flow rate of 0.2 mL/h, with a controlled humidity of 35% at room temperature (20~25°C). The distance between the metal needle and the patch was 9-12 cm. After **es**, the patch was detached from the tin foil and transferred into an oven working at 140°C for 4 hours for high temperature cross-linking of gelatin.

Type I collagen solution (1.7 mg.mL^{-1} in 30 mM HCl and 75 vol% ethanol) was electrospun for 1 hour onto gelatin fibers support at 11 kV with a flow rate of 0.2 mL/h, with a controlled humidity of 25% at room temperature (20∼25°C). The distance between the metal needle and the counter electrode was 11 cm. After **es**, collagen fibrillogenesis was induced in vapor phase by placing the collagen-coated patches in a chamber saturated with ammonia overnight.

2.4 Drop casting (dc). Type I collagen (0.5 mg/mL in PBS, pH=9.0), laminin (10 μg/mL, from Engelbreth-Holm-Swarm murine sarcoma basement membrane) and type IV collagen (0.5 mg/mL, from human placenta) were drop cast by pouring 20 μL of the solution on the patch and dried in air at room temperature.

2.5 SEM imaging. Samples were coated with gold for 60 s with a sputtering current of 50 mA before imaging. Samples were fixed on conductive-tapes for imaging with a TM3030 Tabletop Microscope (Hitachi High-Technologies Corporation, Japan) equipped with TM3030 software and working at an acceleration voltage of 15 kV.

2.6 Second harmonic generation / 2-photon excited fluorescence. We used a custom-built laser-scanning multiphoton microscope and recorded second harmonic generation (SHG) and 2-photon excited fluorescence (2PEF) images in parallel as previously described.[39] Excitation was provided by a femtosecond titanium–sapphire laser (Mai-Tai, Spectra-Physics) tuned to 860 nm, scanned in the XY directions using galvanometric mirrors and focused using a 25× objective lens (XLPLN25X-WMP2, Olympus), with a resolution of 0.35 μm (lateral) × 1.2 μm (axial) and a Z-step of 0.5 μm for the acquisition of Z-stack images. We used circular polarization in order to image all structures independently of their orientation in the image plane, using 100 kHz acquisition rate and 420×420 nm² pixel size.

Patches were observed in duplicate to check for reproducibility and for each patch, three different areas were imaged to verify the homogeneity of the biopolymer coating.

2.7 AFM nanoindentation. AFM experiments were performed on hydrated ECM-models in cell culture medium at room temperature using a NanoWizard 4 (JPK BioAFM, Berlin, Germany) mounted on an Axio Observer microscope (Zeiss, Oberkochen, Germany) placed on a vibration isolation table. Before each experiment, the cantilever spring constant was accurately determined upon calibration in cell culture medium by the thermal noise method.

Young's moduli were determined by colloidal probe force spectroscopy using a gold coated cantilever (0.01 N/m) equipped with a 6.44 µm bead probe (NanoAndMore, Paris, France). Approach and retraction speeds were kept constant at 5 µm/s, ramping the cantilever by 10 µm with a 0.4 nN threshold in a closed z loop. In this option, the feedback system readjusts the initial piezo-position for each force–displacement ramp so that the maximal force applied to the sample remains constant.

AFM force-distance curves were transformed to force-indentation curves and fitted using the JPK data processing software. Curves were fitted using the contact-point independent linear Hertz-Sneddon model. The Hertz model assumes infinite sample thickness, which was approximated by using small indentation (typical indentation depth 500 nm). Automated curve fitting was applied using fitting range of 100% of curve. Force-distance curves were measured in at least 8 positions for 3 different areas of each ECM model.

Statistical analysis was performed using Origin software. Analysis of variance (ANOVA) with the Tukey's Multiple Comparison test was used for all multiple group experiments. P values < 0.05

were deemed significant. Values in graphs are the mean and standard error of mean ($*p < 0.05$, $**p < 0.001$, $***p < 0.0001$).

2.8 Cell culture experiments. SKOV-3 cells (ATCC1, HTB77™), human ovarian adenocarcinoma cell line, were purchased from ATCC (American Type Culture Collection, Manassas, VA). SKOV-3 cells were cultured in RPMI-1640 glutaMAX containing 0.07 % (v/v) sodium bicarbonate supplemented with 10% fetal calf serum and 1% (v/v) penicillin streptomycin (all reagents were purchased from Thermo Fisher Scientific). Cells were cultured in T25 cell culture flasks in a humidified air atmosphere with 5% CO_2 at 37°C.

ECM models were immersed in 70% ethanol for 5 min for sterilization, and washed 3 times for 5 min in sterile PBS. Cells were seeded at a density of 30 000 per patch and cultured for 24 or 48 hours. The cell density was determined after different tests on patches coated with type I collagen (Fig.S1). Patches immersed in cell culture medium were then transferred to a controlled atmosphere (37°C, 5% CO_2) for 1 day.

Experiments were run in triplicate for each ECM condition.

2.9 Immunofluorescence. Cells were fixed in 4% paraformaldehyde (PFA) in PBS for 10 minutes, rinsed three times with PBS. The cells were permeabilized with 0.5% Triton X-100 in PBS, washed again and saturated with PBS containing 3% BSA for 30 min. Cells were incubated overnight at 4°C with Alexa Fluor 543-conjugated vimentin antibody (ab202504, Abcam®) at a 1/1000 dilution. After washing, the actin cytoskeleton was stained with Alexa Fluor 488 Phalloidin in PBS (containing 1% DMSO from the original stock solution, Abcam®) for 40 min at room temperature in a dark chamber. Cell nuclei were then stained with DAPI (4,6-diamidino-2-phenylindole dihydrochloride, Molecular Probe®) for 15 min. Immunofluorescent labelling was observed with

a confocal microscope (LSM710, Zeiss) equipped with 405 (DAPI), 488 (phalloidin), and 543 (anti-vimentin antibody) nm lasers and with LSM ZEN 2009 software. We used 1 μm z-stack intervals and sequential scanning for each wavelength. Images were processed with ImageJ.

For the characterization of the basement membrane by 2PEF, ECM models were stained with Alexa Fluor 488®-conjugated collagen IV monoclonal antibody (eBioscience™, 53-9871-82) incubated overnight at 4°C or 2 h at room temperature at a concentration of 10 $\mu g.mL^{-1}$, together with laminin polyclonal primary antibody (Thermo Fisher Scientific, PA1-16730) overnight at 4°C or 2 h at room temperature at a concentration of 1 $\mu g.ml^{-1}$, followed by 1 to 2 h incubation at room temperature with a goat–anti rabbit-Alexa Fluor 610 secondary antibody at a dilution of 1/250.

2.10. Statistical analysis of cell morphology and image analysis. Cells were analyzed by principal component analysis (PCA) of nucleus morphology.[40,41] We used Celltool[42] to identify single cells based on their nuclei. Experiments were run in triplicate for each ECM condition. The analysis of the morphology of the nucleus was carried out on more than 300 cells per condition, *i.e.* on the triplicate, by considering each cell data as independent. This ensures good sampling of the statistical distribution associated with each microenvironment. PCA allows the determination of the standard deviation (s.d.) that represents the squareroot of the total variance calculated from all the measured morphological features, and hence quantifies the cellular heterogeneity. Custom designed routine in FIJI using macros and python coding were developed to analyze vimentin and actin distribution using line selection tools and plot profile functions.

3. RESULTS

3.1. Biofabrication of ECM models, a combinatorial challenge. The ECM can be described in terms of protein composition, organization and of the resulting mechanical properties such as

stiffness. A first concern to reach physiological stiffness, is that self-supported ECM models should be favored to limit the contribution of the support. This can become challenging when attempting to get biologically relevant thin tissue models. To this aim, we use microfabricated patch supports with a honeycomb pattern (Fig.2A,B), which allows to combine the standing of the ECM model, while leaving large areas of tissue unsupported. One other key advantage of this support compared to conventional solid substrate is its high porosity allowing to preserve the porous features of connective tissues and BM composing the ECM. These patches have been shown to successfully allow the maintenance[43] and differentiation of human induced pluripotent stem cells (hiPSCs) into motor neurons[44] and functional cardiomyocytes,[45] and have been used for various bioassays further underscoring their easy integration into a diversity of devices.[46-50] In this work, for the elaboration of ECM models, circular patches are used having a diameter of 1.1 cm (Fig.2A) with variable dimensions of the honeycomb pattern (Fig.2B yellow arrow). Two dimensions of honeycombs (200 and 400 µm) were tested for the **dc** route to improve the self-standing features of the ECM models and limit the contribution of the support. Note that for the **es** route, only 200 µm patches were used due to the small size of electrospun collagen fibers (see below).

We have selected three ECM proteins that are relevant for investigating the microenvironment of ovarian cancer: type I collagen for the topological changes of connective tissues evidenced in human normal and malignant *ex vivo* biopsies,[26,27] and type IV collagen and laminin for their remodeling in pre-malignant ovarian surface epithelium.[27-30] Independently from the composition, the organization of the connective tissue models was varied using two different processes for type I collagen deposition: electrospinning (**es**) and drop casting (**dc**) (Fig.1). The **es** route leads to the formation of electrospun collagen I nanofibers ($\mathbf{C_{es}}$), eventually topped with a cast layer of laminin

(**LC$_{es}$**) or with successive layers of collagen IV and laminin (**LCC$_{es}$**). Alternatively, in the drop casting route, collagen I is drop cast onto the patch (**C$_{dc}$**), and eventually topped with a layer of laminin (**LC$_{dc}$**) or with successive layers of collagen IV and laminin (**LCC$_{dc}$**) (Fig.1).

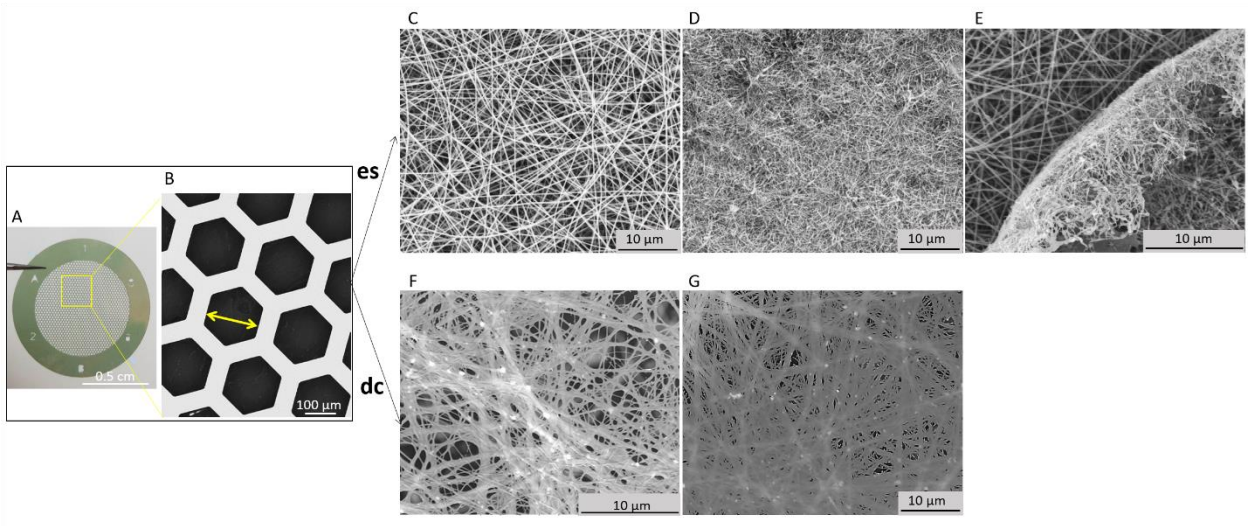

Figure 2. (A) Photograph and (B) SEM image of the microfabricated bare patch. SEM images of patch after electrospinning (**es**) of (C) gelatin, and (D,E) electrospun collagen I on top of the gelatin layer (the image in (E) shows a default on the border of the patch clearly showing the layered structure), and after drop casting (**dc**) collagen I on (F,G) 200 and 400-µm patch respectively.

3.2. Features of ECM models. *3.2.1. Models of connective tissues, structure of type 1 collagen networks.* Scanning electron microscopy (SEM) was used to characterize the formation of the collagen networks by the two routes and compare the topologies obtained by **es** *vs* **dc**. Electrospinning provides a net-like structure made of cross-linked nanofibers and is thus relevant to mimic the complex *in vivo* ECM organization. The process consists in the extrusion of a soluble biopolymer assisted with electrical field. This first requires to coat patch with conductive gold to accumulate collagen fibers on the support (Fig.1A). It has been shown that **es** preserves the native state of collagen I, producing small fibers.[51] Because the collagen nanofibers are small with respect

to the dimension of the honeycomb pattern (*ca*. 70 nm *vs* 200 µm-wide honeycombs), we first deposited a layer of electrospun gelatin (Fig.2C) and did not further increase the size of the honeycomb frame. SEM was used to measure fiber diameter, and estimate the mean pore sizes (detailed analysis of SEM images can be found in supporting information, Fig.S2 and Table S1,S2). For the first step of gelatin electrospinning, fibers were measured to have a mean diameter of 448 nm with a pore size of 2 µm. This layer in turn successfully supports the electrospining of type 1 collagen on the patch (Fig.2D), while preserving the macroporosity of the support. Fig.2D shows the formation of the electrospun network of type 1 collagen having a mean fiber diameter of 72 nm with a mean pore size of 346 nm. This double processing ends with a layered structure of nanofibers (Fig.2E). In parallel, the formation of a network of type 1 collagen was performed by **dc**. Note that before drop casting, patches were coated with gold to keep the mechanical properties of the frame constant with respect to the **es** conditions, and to enhance hydrophilicity of the frame for drop casting. In this case, much larger collagen structures were obtained, with mean diameters of 215 nm whatever the size of the frame, and pore size of 551 and 435 nm respectively for the drop casting on 200- and 400 µm size frame respectively (see Fig.S2 and Table S1,S2). Importantly, the diameters of collagen fibers were in the range 72 to 215 nm, with electrospun scaffold exhibiting the smallest dimensions. This is particularly relevant given that *in vivo* ECM contains fiber diameters ranging from 50 to 500 nm.[52]

Laminin and collagen IV/laminin were then deposited on top of the fibrillar networks showing the formation of a homogeneous film under SEM (Fig.S3-5). Further advanced characterization was done in hydrated bio-compatible conditions using multiphoton microscopy (see next section).

3.2.2. Topology of the ECM models. The nine different ECM models were characterized by multiphoton microscopy combining second harmonic generation (SHG) and 2-photon excited

fluorescence (2PEF). This multimodal imaging allows to monitor in parallel unlabeled collagen I with high specificity towards its fibrillary hierarchical organization through SHG, and collagen IV and laminin after immunostaining using two 2PEF channels. The reproducibility and homogeneity of the biopolymer coating were checked by imaging three different areas for each condition, and prepared as duplicate of patch (in total 6 areas imaged per condition). Figure 3 presents a gallery of SHG/2PEF images with top, bottom and side views for each ECM model.

All scaffolds share common features including a thickness of a couple of microns, and a layer-by-layer structure: for all **LC** and **LCC** scaffolds, the layer structure is confirmed with a bottom collagen I layer (cyan in Fig.3) mimicking connective tissues and a top layer of laminin (magenta in Fig.3) with/without collagen IV (yellow in Fig.3). Side views in Figure 3C,F,I better reveal the layer-by-layer structure in **LCC** scaffolds, as collagen IV signal is difficult to identify on 3D reconstructions due to its embedding in between collagen I and laminin. The presence of collagen IV was further evidenced by the single 2PEF channel image as shown for **LCC$_{dc}$** (Fig.3J and see also Supporting Information for the full characterization of all the ECM models, Fig.S6).

The scaffolds obtained by the **dc** route, whatever the dimension of honeycombs, are qualitatively similar with flat, layered structures based on a bottom fibrillar network of collagen I (Fig.3D-I). Topologic variations specific to the process can be observed with electrospun scaffolds: (1) **es** scaffolds are not as planar as the **dc** ones (Fig.3A-C). This is attributed to the heterogeneous distribution of the electric field throughout the patch used for **es**: the electric field is not constant over the patch due to the presence of the gold frame and of empty honeycombs. (2) The structure of the collagen I network is very specific to the process, *i.e.* **es** *vs* **dc**, which is better evidenced when comparing the pure collagen I scaffolds (see **C$_{es}$** *vs* **C$_{dc}$** scaffolds, Fig.3A and D,G). The **es** scaffolds exhibited a grainy-like pattern with alternating high and low SHG intensity. As it has

been reported earlier, this signs for the small size of the fibrils with high entanglement.[51] Indeed, given that the diameter of the fibrils (*ca*. 70 nm) is small relatively to the focal volume (0.35 µm (lateral) × 1.2 µm (axial)), many fibrils may be simultaneously observed in one pixel. At the intersection of these fibrils, a centrosymmetric distribution of the molecules is obtained in the focal volume, which leads to a local decrease of SHG signal.[51] If the network is highly entangled, SHG decrease is widespread throughout the focal volume leading to a grainy-like image (Fig.3A). In contrast, after drop casting, collagen I networks are made up of large entangled fibrils, as observed in Figure 3D and G.[53]

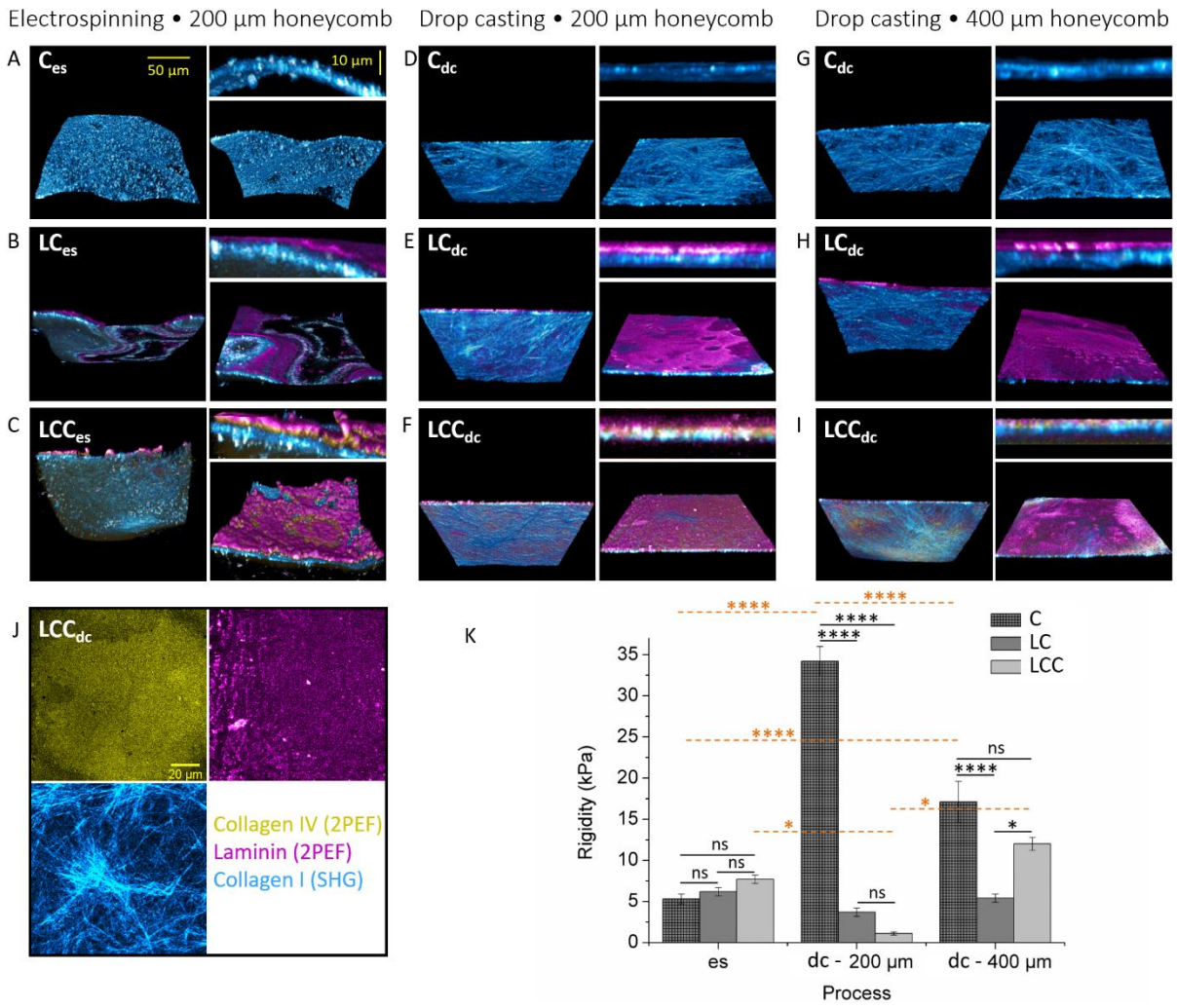

Figure 3. SHG (collagen I in cyan) and 2PEF (laminin in magenta and collagen IV in yellow) images of the ECM models after (A-C) **es** and **dc** on (D-F) 200 µm- and (G-I) 400 µm-honeycombs. For each sample, the left image is the bottom view, the top right one the side view, and the bottom right image is the top view. The underlying gelatin layer is not stained. (J) Details of the single channels recorded for multiphoton characterization of the **LCC$_{dc}$** sample: top left is the 2PEF channel for anti-collagen IV antibody detection (in yellow), top right is the 2PEF channel for the anti-laminin antibody detection (in magenta) and the bottom left is the SHG channel for unstained collagen I detection (in cyan). (K) Mean Young's modulus values for all ECM models measured by peak force tapping AFM-nanoindentation. In the plots, the column represents Mean with SEM. ($*p < 0.05$, $***p < 0.00001$, ns for non-significant; using Tukey's Multiple Comparison test).

3.2.3 Mechanical properties. Nanoindentation was implemented by peak force tapping AFM in liquid environment This is particularly powerful for characterizing soft biomaterials with nanometer depth and picoNewton force resolution.[54-59] To measure quantitatively the mechanical heterogeneity of ECM stiffness, the median of Young's modulus values was measured in at least 8 positions for 3 different areas for each type of scaffold. Here, we observed median Young's modulus values in the 1 to 35 kPa range (Fig. 3K and Table S3). The lower so-called "soft" values in the kPa order are similar to what is measured from physiological ECM, while the higher "stiff" values with tens of kPa have been associated with severe diseases such as cancer and fibrosis.[60-62] **es** scaffolds were found to be soft and homogeneous (see Table S3). Non-significant variations in Young's moduli were measured after addition of laminin and collagen IV (5.3 to 6.2 and 7.7 kPa) (Fig.3K). In contrast, after drop casting of collagen I, stiff scaffolds were obtained (34.2 and 17.1 kPa on 200 and 400-µm patch respectively) and exhibited higher heterogeneity than **es** scaffolds.

This is attributed to the formation of the large bundles of drop cast collagen I as observed by SEM and SHG that accounts for both higher stiffness and higher local heterogeneity when compared to the more homogeneous networks of small collagen fibers obtained by **es**. At this point, it is worth discussing the impact of the gelatin layer underlying the electrospun network of type 1 collagen (**C_{es}** in Fig.1A and Fig.2E). To assess its potential contribution to the mechanical properties, measurements were performed on electrospun gelatin samples without any coating (**200-$Gelatin_{es}$**, table S3) and after drop casting of type 1 collagen (**200-$Gelatin_{es}C_{dc}$**, table S3). Young moduli of 3.7 and 35.8 kPa were measured respectively. These two different values first indicate that the addition of drop cast collagen I dominates over the presence of the electrospun gelatin network. Second, the similarity of the Young moduli obtained for **200-$Gelatin_{es}C_{dc}$** and for **200-C_{dc}** (35.8 *vs* 34.2 kPa respectively) confirms the conclusion that drop casting of type 1 collagen dominates the mechanical properties of the resulting ECM models, the contribution of the electrospun gelatin being negligible for the resulting mechanical properties. By extension, the contribution of the underlying gelatin layer on the stiffness of **es** scaffolds was ruled out. The difference in Young moduli measured between **C_{es}** on one hand, and **200-C_{dc}** and **400-C_{dc}** on the other hand cannot be attributed to the presence of the gelatin layer in **C_{es}** samples. This indicates that for indentation depth of the scale of indentation by the cell (500 nm), the choice of **es** *vs* **dc** dominates the resulting topology and stiffness of ECM models.

For drop cast scaffolds, the addition of laminin or collagen IV-laminin, softens significantly the scaffold, with Young's modulus values droping from 34.2 to 3.7 and 1.1 kPa respectively for 200 µm-wide honeycombs and from 17.1 to 5.4 and 12 kPa for 400 µm-wide honeycombs. In addition to their softening, the ECM scaffolds appear much more homogeneous in terms of stiffness distribution. This is attributed to the formation of the BM layer identified by SEM and 2PEF,

compared to the large collagen bundles associated to a high stiffness and heterogeneity obtained by **dc**.

One step further, we examine the impact of the process and patch dimensions on stiffness for a given protein composition (in orange in Fig.3K; for clarity, only significant differences have been marked, and see also Table S4). No significant difference in Young's moduli were measured between **LC** scaffolds contrary to **LCC**. In addition, the most important differences in Young's moduli were observed for pure collagen I scaffolds, the **es** one being the softest. Changing process leads to different protein organizations and topology (Fig.3A,D,G) and to different stiffness. Moreover, significant differences were measured for drop cast collagen on 200 and 400 µm pattern going respectively from 34.2 to 17.1 kPa. This shows that playing with the dimensions of the patch support is an efficient way of tuning stiffness independently from the topology of collagen I fibers, and independently from the protein composition.

3.3. Impact of the ECM model on ovarian cancer cells. The possibility to generate the cellular heterogeneity associated with ovarian cancer has been assessed on the different ECM models. Human ovarian adenocarcinoma SKOV-3 cell line has been selected for modelling cellular heterogeneity because their phenotypes *in vitro* are representative of the heterogeneity observed in ovarian cancer.[21-24] Cells were seeded at a density of 30 000 per patch and cultured for 24 or 48 hours. The cell density was determined after different tests on patches coated with type I collagen (Fig.S1).

The evolution of cell phenotypes on the different ECM models was monitored by immunofluorescence. Experiments were run in triplicate and nucleus morphology analysis was carried out on more than 300 cells per condition. Cells were stained for the nucleus (DAPI) and

for the cytoskeleton by combining staining of actin (phalloidin) and of vimentin (anti-vimentin antibody). Vimentin is a cytoskeletal protein upregulated during cell transitioning events commonly used as a marker of the epithelial-to-mesenchymal transition (EMT) that see epithelial cells evolving towards less cohesive and highly motile cells,[3-6] and whose expression is associated with mesenchymal phenotypes. Confocal microscopy observations revealed important phenotypic variations depending on the ECM models. Two extreme phenotypes can be described, together with a multiplicity of intermediary states. First, cells with a compact and round nucleus were identified, which is characteristic of most epithelial cells (Fig.4A). This is also associated with a perinuclear distribution of vimentin as clearly identified in Figure 4A4. On the other side of the phenotypic continuum, elongated cells having a spindle-like morphology were also observed (Fig.4B). These cells exhibited an elongated actin cytoskeleton. Remarkably the cortical distribution of vimentin is observed, which drastically differs from the epithelial-type of cells described previously. In that case, the vimentin cytoskeleton co-localizes with the actin one (Fig.4B4). This is characteristic of mesenchymal-type cells. This has been confirmed by quantitative analysis, where we have extracted the intensity profile of vimentin and actin throughout the whole cell length. Localization statistics were performed on more than 100 cells. This analysis shows that vimentin expression is homogeneously distributed over the whole normalized position along the length of cells with rather epithelial phenotype (Fig.4C, in blue), contrary to what is observed with more mesenchymal type cells (Fig.4C, in orange). In addition, this statistical analysis indicates similar vimentin and actin localization over the cell length of mesenchymal cells (see Fig.4C and D, in orange), contrary to what is observed with more epithelial cells (Fig.4C and D, in blue). This illustrates the high level of reorganization of cells and shows the influence of the ECM microenvironment on cytoskeleton reorganization. Importantly, it also

confirms the possibility to generate cellular heterogeneity in ovarian cancer cells based on the alteration of the scaffold microenvironment only. This was confirmed by immunofluorescence staining of E-cadherin, the expression of which is known to be strongly affected depending on epithelial and mesenchymal phenotypes (Fig.S7-S9).

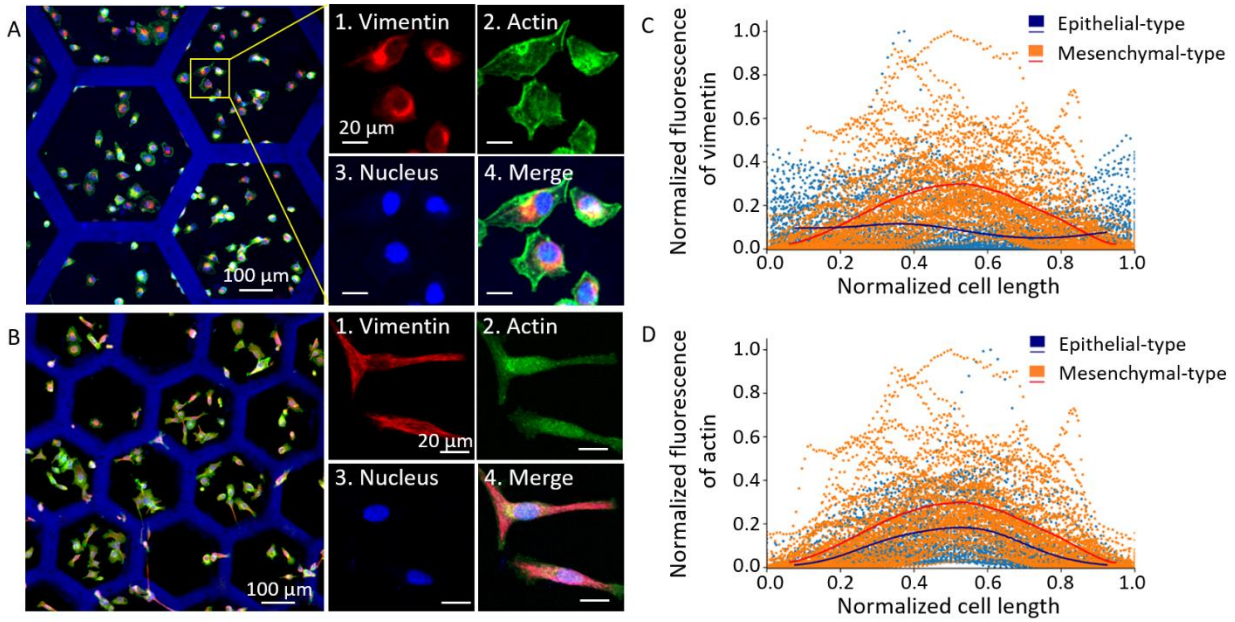

Figure 4. Immunofluorescence images of SKOV-3 cells one day after seeding on (A) **400-C$_{dc}$** and (B) **200-LCC$_{dc}$**. Cells were stained for (1) vimentin (red), (2) actin (green), and (3) nuclei (blue); (4) is the merge of the three. The scale bar is 20 µm for all zoom-in images. (C,D) Normalized fluorescence of vimentin and actin integrated over the whole normalized position along the cell length. A Kruskal Wallis test over more than 100 cells shows the significant difference in distribution of vimentin in epithelial-type cells (from a **400-C$_{dc}$** scaffold, see (A)) and rather mesothelial-type cells (from a **200-LCC$_{dc}$** scaffold, see (B)) ($p = 0.0001$).

We then quantified these changes in morphology at the cell level by automated object segmentation and measurement using principal component analysis (PCA), over 10 000

cells.[40,41,63] We focused on shape metrics because it is less prone to external contributions when compared to the analysis of fluorescence intensity of specific markers (staining, acquisition conditions). We identified cells based on their nuclei, since nuclei are mechanosensors of external ECM cues.[31,63] Based on the segmentation of nuclei, two parameters, called modes, were found to recapitulate the cellular heterogeneity generated on the ECM models. Figures 5A1 and B1 show the two corresponding histograms that represent the spectrum of diversity for all segmented nuclei (the color code is common to A1 and B1). Shape mode 1 mostly accounts for the size of the nucleus and represents 90% of total variance (Fig.5A1). Shape mode 2 represents nucleus shape. It accounts for 7.9% of variability (Fig.5B1). The corresponding mean values and distributions of nucleus size and shape as a function of ECM models are further detailed in Figures 5A2 and B2 respectively.

Let us first examine the heterogeneity in nucleus size. Figure 5A2 shows that nucleus sizes measured over more than 300 cells per condition were found to be significantly different when comparing all ECM models with each other. Remarkably, no specific trend could be identified with respect to the protein composition within each of the three groups of scaffolds. A small increase in size was observed from $\mathbf{C}_{\mathbf{es}}$ to $\mathbf{LC}_{\mathbf{es}}$ and to $\mathbf{LCC}_{\mathbf{es}}$. The inverse trend was observed for 400-drop cast samples and no common features identified with 200-drop cast samples. In contrast, significant trends were observed when comparing **es** *vs* **dc** routes. Cells on **es** scaffolds (yellow box, Fig.5A2) displayed compact nuclei whatever the protein composition, when compared to cells seeded on drop cast scaffolds with either 200 or 400 µm dimensions. In these later cases, much larger nuclei were measured. This is an interesting result given that the most important difference when comparing the three groups is the topology of reconstructed connective tissues from type I collagen (see SHG in Fig.3A-I) rather than the stiffness (except for the pure $\mathbf{C}_{\mathbf{es/dc}}$). Importantly,

this could further be confirmed when SKOV-3 cells were left to transition over 48 h (Fig.S10). Again, significantly smaller nuclei were measured on **es** scaffolds whatever the protein composition compared to **dc** scaffolds. The importance of topology over stiffness is also illustrated when comparing **LC$_{es}$**, **200-LC$_{dc}$** and **400-LC$_{dc}$** that exhibit similar stiffness and protein composition but different connective tissues topology resulting in important variations of the nucleus size (yellow arrows, Fig.5A2, and see also the immunofluorescence images in Fig.S11).

Changes in shape mode 2 mostly account for the deformation of nucleus. In that case, non-significant nucleus deformations were measured for **es** scaffolds, and when comparing **200-C$_{dc}$** and **200-LC$_{dc}$** (Fig.5B2). The most important deformations of the nucleus were measured on **LCC$_{dc}$** models, *i.e.* for given topology and protein composition, but different stiffness of the ECM models (yellow arrows, Fig.5B2).

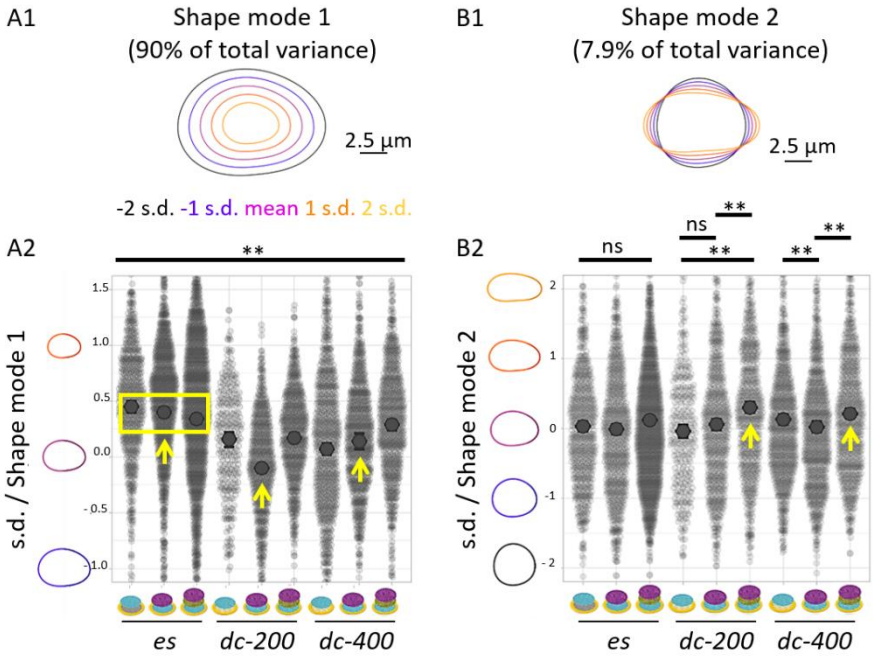

Figure 5. Principal component analysis of nucleus morphology one day after seeding on the different ECM models: morphological variance for (A1-2) shape mode 1 – nucleus size mostly –

and (B1-2) shape mode 2 – nucleus shape (comparison is between all samples for A2 and between samples at extremities of bar in B2, with n.s: non-significant; *p<0.05; **p<0.001). The color code is common to A1 and B1. s.d. in A1,2 and B2 is for standard deviation, as determined by PCA for the quantification of the variance in the measured morphological features. All plots were realized using SuperPlotsOfData.[64]

4. DISCUSSION

4.1. Recapitulating native ECM. Because cells respond to their microenvironment, including mechanical and biochemical cues from the ECM, it is important to discriminate protein composition, topology and ECM stiffness to deepen our understanding and improve the biofabrication of relevant *in vitro* models. Here we have elaborated a library of ECM models, where not only stiffness and ECM composition but also the topology of connective tissues could be varied. This ability to adjust ECM models to meet different requirements is crucial given the constant remodeling of the ECM, as described by SHG/2PEF from *ex vivo* ovarian biopsies cancer.[26,27] Using SEM, SHG/2PEF and AFM nanoindentation, we have characterized the composition, topology and stiffness of nine different ECM models obtained from ECM proteins. All reproduce the native topology of connective tissues (72 to 215 nm fiber diameters) with a top basement membrane and biological stiffness (1 to 35 kPa). First playing with the processing of biomolecules (**es** *vs* **dc**), we have shown that the method used to process type I collagen controls the topology and associated stiffness of the connective tissues. In this case, composition and matrix topology can be varied independently, BM proteins being drop cast on already shaped collagen fibers. Interestingly, from these connective tissue models, the addition of an artificial BM was found to soften the ECM, and this independently from collagen I process. Second, by varying the dimensions of the microfabricated supports, the stiffness can be decoupled from collagen topology,

and also from the composition in ECM proteins. This makes our ECM models prone to mimic a given tissue and different physiological contexts.

4.2. Scaffold-induced cellular heterogeneity. Two important results must be emphasized here: (1) a clear difference in cell morphology is observed on different ECM models. A high degree of cytoskeleton reorganization, revealed by the variation of vimentin distribution, is triggered only playing with the scaffold. (2) The quantification of cellular heterogeneity generated by the ECM models revealed that the evolution of SKOV-3 morphology could be recapitulated by two modes defining the evolution of the size and shape of the nucleus. Both metrics – size and shape of nuclei – were found not to evolve concomitantly for all ECM models. This is remarkable *per se* and may be attributed to the existence of different mechanotransduction pathways[3] differently balanced over the ECM models. Moreover, the different patterns of evolution between shape mode 1 and 2 are probably at the origin of cellular heterogeneity, where different subpopulations of tumor cells with hybrid phenotypes were identified.[65] Ultimately, our strategy offers the possibility to generate a broad diversity of phenotypic variations to be isolated on defined ECM models that take into account the biochemistry, mechanical properties, and topology of the microenvironment for further mechanistic investigations.

4.3. The importance of the topology of connective tissues. Very importantly, the results also highlight the absence of a direct trend between nucleus size/deformation and the ECM features. This highlights the multidimensional correlation of the different biophysical and biochemical cues that cannot be restricted to one varying parameter, not even the stiffness.[35] This can explain the controversy found in literature on the dependency of SKOV-3 cell fate with stiffness. SKOV-3 cells are clinically defined as having an epithelial morphology.[66] Different groups have reported that soft matrices promote transitioning from epithelial to mesenchymal type cells, and the

acquisition of mesenchymal spindle-like cell shape together with the increase in vimentin expression.[67,68] In contradiction, others have shown that increasing stiffness is associated with cell spreading and migration.[69] All these works concern the same cell line and stiffness range but with no concern on protein nature and topology. Our strength in providing combinatorial ECM models is that it allows to discuss protein composition, topology and stiffness in a single study in which the systems are directly comparable, which cannot be achieved when comparing results coming from different works and strategies. Still, our results indicate that the use of **es** is correlated to a soft ECM (5.3 to 7.7 kPa), small nuclei (Fig.5A) and low deformation (Fig.5B). This is attributed to the 3D collagen fibril topology that can shape the morphology of cells, as recently discussed by Ranamukhaarachchi.[15] Indeed, as collagen I processing allows controlling the diameter of the fibers, **es** ECMs exhibit significantly smaller diameter and rather induce epithelial-type cells with smaller size of nuclei than **dc** scaffolds. Importantly, this could further be confirmed when SKOV-3 cells were left to transition over 48 h (Fig.S10). Importantly, the 3D topology may also include the curvotaxis of **es** scaffold, revealed by SHG, as opposed to the more planar **dc** models, which has been previously shown to affect cell-ECM interactions.[70] Topology is a parameter, which has been quite underestimated for years and must systematically be taken into account when biofabricating tissue models.

5. CONCLUSION

We have built *in vitro* models that recapitulate the biochemical, mechanical and topological characteristics of the cell microenvironment. ECM models reproducing both the scaffold of connective tissues and basement membrane allow to investigate the interplay between protein composition, topology and stiffness in generating cellular heterogeneity in SKOV-3 cells. These cellular changes in response to ECM cues resemble many morphological features associated with

EMT. In particular, ECM models with small fiber diameters were found to favor the generation of epithelial-type cells, independently from the stiffness. This generates new knowledge on cell heterogeneity in cancer, where the topology of connective tissues was found to impact nucleus size and shape independently of stiffness and protein composition. This is particularly important given the importance of ECM features in generating cellular heterogeneity, and the in turn impact of heterogeneity in resistance to chemotherapy. As such, our results provide *in vitro* models that better mimic the ECM, including topology with specificity for tissues and disease stage, which will certainly be a gain in cancer model engineering and drug testing.

ASSOCIATED CONTENT

Supporting Information. The following files are available free of charge. Microfabrication of the patches. Determination of the cell seeding density. Features of ECM models: Analysis of the SEM imaging of collagen networks: fiber diameter and pore size; SEM imaging of the deposition of an artificial basement membrane; Second harmonic generation/2-photon excited fluorescence; AFM nanoindentation. Characterization of cellular heterogeneity by immunofluorescence and E-cadherin staining. SKOV-3 evolution over two days. The importance of topology over stiffness, immunofluorescence imaging.

AUTHOR INFORMATION

Corresponding Author

* ambroise.lambert@u-cergy.fr

* carole.aime@ens.psl.eu

Author Contributions

The manuscript was written through contributions of all authors. All authors have given approval to the final version of the manuscript.

ACKNOWLEDGMENT

We thank the China Scholarship Council for the PhD grant of Changchong Chen, Christophe Hélary and Gervaise Mosser for their help in the extraction and purification of type I collagen, and Clothilde Raoux for her constant support with SHG/2PEF experiments. This project has received financial support from the CNRS through the MITI interdisciplinary programs. Multiphoton imaging at LOB was partly supported by the Agence Nationale de la Recherche (contract ANR-10-INBS-04 France BioImaging and ANR-11-EQPX-0029 Morphoscope2). This work benefited from the technical contribution of the Institut Pierre-Gilles de Gennes joint service unit CNRS UAR 3750. The authors would like to thank the engineers of this unit for their advice during the development of the experiments: Bertrand Cinquin, Nhung Dinh, Audric Jan, Kévin Phan. We thank members of MEC-uP Team for helpful discussions and comments. Johanne Leroy-Dudal and Rémy Agniel for experimental discussions. This work was funded by CY Initiative of Excellence (grant "Investissements d'Avenir" ANR-16-IDEX-0008).

REFERENCES

(1) Kessler, D. A.; Austin, R. H.; Levine, H. Resistance to chemotherapy: patient variability and cellular heterogeneity. *Cancer Res*. **2014**, *74*, 4663-4670. DOI:10.1158/0008-5472.CAN-14-0118.

(2) Frantz, C.; Stewart, K. M.; Weaver, V. M. The extracellular matrix at a glance. *J. Cell Sci.* **2010**, *123*, 4195-4200. DOI:10.1242/jcs.023820.

(3) Wei, S. C.; Fattet, L.; Tsai, J. H.; Guo, Y.; Pai, V. H.; Majeski, H. E.; Chen, A. C.; Sah, R. L.; Taylor, S. S.; Engler, A. J.; Yang, J. Matrix stiffness drives epithelial-mesenchymal transition and tumour metastasis through a TWIST1-G3BP2 mechanotransduction pathway. *Nat. Cell Biol.* **2015**, *17*, 678-688. DOI:10.1038/ncb3157.

(4) Rice, A. J.; Cortes, E.; Lachowski, D.; Cheung, B. C. H.; Karim, S. A.; Morton, J. P.; Del Río Hernández, A. Matrix stiffness induces epithelial-mesenchymal transition and promotes chemoresistance in pancreatic cancer cells. *Oncogenesis* **2017**, *6*, e352. DOI:10.1038/oncsis.2017.54.

(5) Matte, B. F.; Kumar, A.; Placone, J. K.; Zanella, V. G.; Martins, M. D.; Engler, A. J., Lamers, M. L. Matrix stiffness mechanically conditions EMT and migratory behavior of oral squamous cell carcinoma. *J. Cell Sci.* **2019**, *132*, jcs224360. DOI: 10.1242/jcs.224360.

(6) Dong, Y.; Zheng, Q.; Wang, Z.; Lin, X.; You, Y.; Wu, S.; Wang, Y.; Hu, C.; Xie, X.; Chen, J.; Gao, D.; Zhao, Y.; Wu, W.; Liu, Y.; Ren, Z.; Chen, R.; Cui, J. Higher matrix stiffness as an independent initiator triggers epithelial-mesenchymal transition and facilitates HCC metastasis. *J. Hematol. Oncol.* **2019**, *12*, DOI:112. 10.1186/s13045-019-0795-5.

(7) Ondeck, M. G.; Kumar, A.; Placone, J. K.; Plunkett, C. M.; Matte, B. F.; Wong, K. C.; Fattet, L.; Yang, J.; Engler, A. J. Dynamically stiffened matrix promotes malignant transformation of mammary epithelial cells via collective mechanical signaling. *Proc. Natl. Acad. Sci. U.S.A.* **2019**, *116*, 3502. DOI: 10.1073/pnas.1814204116.

(8) Fattet, L.; Jung, H.-Y.; Matsumoto, M. W.; Aubol, B. E.; Kumar, A.; Adams, J. A.; Chen, A. C.; Sah, R. L.; Engler, A. J.; Pasquale, E. B.; Yang, J. Matrix Rigidity Controls Epithelial-Mesenchymal Plasticity and Tumor Metastasis via a Mechanoresponsive EPHA2/LYN Complex. *Dev. Cell*. **2020**, *54*, 302-316. DOI: 10.1016/j.devcel.2020.05.031.

(9) Lv, Y.; Wang, H.; Li, G.; Zhao, B. Three-dimensional decellularized tumor extracellular matrices with different stiffness as bioengineered tumor scaffolds. *Bioact. Mater.* **2021**, *6*, 2767-2782. DOI:10.1016/j.bioactmat.2021.02.004.

(10) Barriga, E. H.; Franze, K.; Charras, G.; Mayor, R. Tissue stiffening coordinates morphogenesis by triggering collective cell migration in vivo. *Nature*, **2018**, *554*, 523-527. DOI: 10.1038/nature25742.

(11) Tzanakakis, G.; Kavasi, R. M.; Voudouri, K.; Berdiaki, A.; Spyridaki, I.; Tsatsakis, A.; Nikitovic, D. Role of the extracellular matrix in cancer-associated epithelial to mesenchymal transition phenomenon. *Dev Dyn.* **2018**, *247*, 368-381. DOI:10.1002/dvdy.24557.

(12) Jokela, T. A.; LaBarge, M. A. Integration of mechanical and ECM microenvironment signals in the determination of cancer stem cell states. *Curr. Stem Cell Rep.* **2021**, *7*, 39-47. DOI: 10.1007/s40778-020-00182-2.

(13) Scott, L. E.; Weinberg, S. H.; Lemmon, C. A. Mechanochemical Signaling of the Extracellular Matrix in Epithelial-Mesenchymal Transition. *Front Cell Dev Biol.* **2019**, *7*, 135. DOI: 10.3389/fcell.2019.00135.

(14) Baker, B. M.; Trappmann, B.; Wang, W. Y.; Sakar, M. S.; Kim, I. L.; Shenoy, V. B.; Burdick, J. A.; Chen, C. S. Cell-mediated fibre recruitment drives extracellular matrix mechanosensing in engineered fibrillar microenvironments. *Nat Mater*. **2015**, *14*, 1262-1268. DOI: 10.1038/nmat4444.

(15) Huang, G.; Wang, L.; Wang, S.; Han, Y.; Wu, J.; Zhang, Q.; Xu, F.; Lu, T. J. Engineering three-dimensional cell mechanical microenvironment with hydrogels. *Biofabrication* **2012**, *4*, 042001. DOI: 10.1088/1758-5082/4/4/042001.

(16) Antoine, E. E.; Vlachos, P. P.; Rylander, M. N. Review of collagen I hydrogels for bioengineered tissue microenvironments: characterization of mechanics, structure, and transport. *Tissue Eng Part B Rev.* **2014**, *20*, 683-696. DOI: 10.1089/ten.TEB.2014.0086.

(17) Shi, N.; Li, Y.; Chang, L.; Zhao, G.; Jin, G.; Lyu, Y.; Genin, G. M.; Ma, Y.; Xu, F. A 3D, Magnetically actuated, aligned collagen fiber hydrogel platform recapitulates physical microenvironment of myoblasts for enhancing myogenesis. *Small Methods* **2021**, *5*, 2100276. DOI: 10.1002/smtd.202100276.

(18) Montanez-Sauri, S. I.; Eun Sung, K.; Berthier, E.; Beebe, D. J. Enabling Screening in 3D Microenvironments: Probing Matrix and Stromal Effects on the Morphology and Proliferation of T47D Breast Carcinoma Cells. *Integr Biol (Camb)* **2013**, *5*, 631-640. DOI:10.1039/c3ib20225a.

(19) Ranamukhaarachchi, S. K.; Modi, R. N.; Han, A.; Velez, D. O.; Kumar, A.; Engler, A. J.; Fraley, S. I. Macromolecular crowding tunes 3D collagen architecture and cell morphogenesis. *Biomater. Sci.* **2019**, *7*, 618-633. DOI: 10.1039/c8bm01188e.

(20) Bascetin, R.; Laurent-Issartel, C.; Blanc-Fournier, C.; Vendrely, C.; Kellouche, S.; Carreiras, F.; Gallet, O.; Leroy-Dudal, J. A biomimetic model of 3D fluid extracellular macromolecular crowding microenvironment fine-tunes ovarian cancer cells dissemination phenotype. *Biomaterials*. **2021**, *269*, 120610. DOI: 10.1016/j.biomaterials.2020.120610.

(21) Strauss, R.; Li, Z.-Y.; Liu, Y.; Beyer, I.; Persson, J.; Sova, P.; Möller, T.; Pesonen, S.; Hemminki, A.; Hamerlik, P.; Drescher, C.; Urban, N.; Bartek, J.; Lieber, A. Analysis of epithelial and mesenchymal markers in ovarian cancer reveals phenotypic heterogeneity and plasticity *PLoS ONE*. **2011**, *6*, e16186. DOI: 10.1371/journal.pone.0016186.

(22) Huang, R. Y.-J.; Wong, M. K.; Tan, T. Z.; Kuay, K. T.; Ng, A. H. C.; Chung, V. Y.; Chu, Y.-S.; Matsumura, N.; Lai, H.-C.; Lee, Y. F.; Sim, W.-J.; Chai, C.; Pietschmann, E.; Mori, S.; Low, J. J. H.; Choolani, M.; Thiery, J. P. An EMT spectrum defines an anoikis-resistant and spheroidogenic intermediate mesenchymal state that is sensitive to e-cadherin restoration by a src-kinase inhibitor, saracatinib (AZD0530). *Cell Death Dis.* **2013**, *4*, e915. DOI: 10.1038/cddis.2013.442.

(23) Tan, T. Z.; Miow, Q. H.; Huang, R. Y.-J.; Wong, M. K.; Ye, J.; Lau, J. A.; Wu, M. C.; Hadi, L. H. B. A.; Soong, R.; Choolani, M.; Davidson, B.; Nesland, J. M.; Wang, L.-Z.; Matsumura, N.; Mandai, M.; Konishi, I.; Goh, B.-C.; Chang, J. T.; Thiery, J. P.; Mori, S. Functional genomics identifies five distinct molecular subtypes with clinical relevance and pathways for growth control in epithelial ovarian cancer. *EMBO Mol. Med.* **2013**, *5*, 1051-1066. DOI: 10.1002/emmm.201201823.

(24) Carduner, L.; Leroy-Dudal, J.; Picot, C.R.; Gallet, O.; Carreiras, F.; Kellouche, S. Ascites-induced shift along epithelial-mesenchymal spectrum in ovarian cancer cells: enhancement of

their invasive behavior partly dependant on αv integrins. *Clin Exp Metastasis.* **2014**, *31*, 675-688. DOI: 10.1007/s10585-014-9658-1.

(25) Feldman, G. B.; Knapp, R. C.; Order, S. E.; Hellman, S. The role of lymphatic obstruction in the formation of ascites in a murine ovarian carcinoma. *Cancer Res*. **1972**, *32*, 1663-1666.

(26) Stenbäck, F.; Wasenius, V.-M. Basement membrane structures in tumors of the ovary. *Eur. J. Obstet. Gynec. Reprod. Biol.* **1985**, *20*, 357-371. DOI: 10.1016/0028-2243(85)90059-0.

(27) Yang, D.-H.; Smith, E. R.; Cohen, C.; Wu, H.; Patriotis, C.; Godwin, A. K.; Hamilton, T. C.; Xu, X.-X. Molecular events associated with dysplastic morphologic transformation and initiation of ovarian tumorigenicity. *Cancer*. **2002**, *94*, 2380-2392. DOI: 10.1002/cncr.10497.

(28) Roland, I. H.; Yang, W.-L.; Yang, D.-H.; Daly, M. B.; Ozols, R. F.; Hamilton, T. C.; Lynch, H. T.; Godwin, A. K.; Xu, X.-X. Loss of surface and cyst epithelial basement membranes and preneoplastic morphologic changes in prophylactic oophorectomies. *Cancer*. **2003**, *98*, 2607-2623. DOI: 10.1002/cncr.11847.

(29) Nadiarnykh, O.; LaComb, R. B.; Brewer, M. A.; Campagnola, P. J. Alterations of the extracellular matrix in ovarian cancer studied by Second Harmonic Generation imaging microscopy. *BMC Cancer*. **2010**, *10*, 94. DOI: 10.1186/1471-2407-10-94.

(30) Kirkpatrick, N. D.; Brewer, M. A.; Utzinger, U. Endogenous optical biomarkers of ovarian cancer evaluated with multiphoton microscopy. *Cancer Epidemiol Biomarkers Prev*. **2007**, *16*, 2048-2057. DOI: 10.1158/1055-9965.EPI-07-0009.

(31) Sero, J. E.; Sailem, H. Z.; Ardy, R. C.; Almuttaqi, H.; Zhang, T.; Bakal, C. Cell shape and the microenvironment regulate nuclear translocation of NF-κB in breast epithelial and tumor cells. *Mol Syst Biol*. **2015**, *11*, 790. DOI: 10.15252/msb.20145644.

(32) Zink, D.; Fischer, A. H.; Nickerson, J. A. Nuclear structure in cancer cells. *Nat Rev Cancer*. **2004**, *4*, 677-687. DOI: 10.1038/nrc1430.

(33) Verdone, J. E.; Parsana, P.; Veltri, R. W.; Pienta, K. J. Epithelial-mesenchymal transition in prostate cancer is associated with quantifiable changes in nuclear structure. *Prostate*. **2015**, *75*, 218-224. DOI: 10.1002/pros.22908.

(34) Fisher, E. G. Nuclear Morphology and the Biology of Cancer Cells. *Acta Cytologica*. **2020**, *64*, 511-519. DOI: 10.1159/000508780.

(35) Micalet, A.; Moeendarbary, E.; Cheema, U. 3D *In Vitro* Models for Investigating the Role of Stiffness in Cancer Invasion. *ACS Biomater. Sci. Eng.* **2021**. DOI: 10.1021/acsbiomaterials.0c01530.

(36) Gobeaux, F.; Mosser, G.; Anglo, A.; Panine, P.; Davidson, P.; Giraud-Guille, M.-M.; Belamie, E. Fibrillogenesis in dense collagen solutions: a physicochemical study. *J. Mol. Biol.* **2008**, *376*, 1509-1522. DOI: 10.1016/j.jmb.2007.12.047.

(37) Giraud-Guille, M.-M.; Besseau, L.; Herbage, D.; Gounon, P. Optimization of Collagen Liquid Crystalline Assemblies: Influence of Sonic Fragmentation. *J. Struct. Biol.* **1994**, *113*, 99-106.

(38) Bergman, I.; Loxley, R. Two Improved and Simplified Methods for the Spectrophotometric Determination of Hydroxyproline. *Anal. Chem.* **1963**, *35*, 1961-1965.

(39) Teulon, C.; Tidu, A.; Portier, F.; Mosser, G.; Schanne-Klein, M.-C. Probing the 3D structure of cornea-like collagen liquid crystals with polarization-resolved SHG microscopy. *Opt. Express.* **2016**, *24*, 16084-16098. DOI:10.1364/OE.24.016084.

(40) Pincus, Z.; Theriot, J. A. Comparison of quantitative methods for cell-shape analysis. *J. Microscopy.* **2007**, *227*, 140-156. DOI: 10.1111/j.1365-2818.2007.01799.x.

(41) Lambert, A.; Vanhecke, A.; Archetti, A.; Holden, S.; Schaber, F.; Pincus, Z.; Laub, M. T.; Goley, E.; Manley, S. Constriction Rate Modulation Can Drive Cell Size Control and Homeostasis in C. crescentus. *iScience*. **2018**, *4*, 180-189. DOI:10.1016/j.isci.2018.05.020.

(42) McQuin, C.; Goodman, A.; Chernyshev, V.; Kamentsky, L.; Cimini, B. A.; Karhohs, K. W.; Doan, M.; Ding, L.; Rafelski, S. M.; Thirstrup, D.; Wiegraebe, W.; Singh, S.; Becker, T.;

Caicedo, J. C.; Carpenter, A. E. CellProfiler 3.0: Next-generation image processing for biology. *PLoS Biol.* **2018**, *16*, e2005970. DOI:10.1371/journal.pbio.2005970.

(43) Liu, L.; Kamei, K.-I.; Yoshioka, M.; Nakajima, M.; Li, J.; Fujimoto, N.; Terada, S.; Tokunaga, Y.; Koyama, Y.; Sato, H.; Hasegawa, K.; Nakatsuji, N.; Chen, Y. Nano-on-micro fibrous extracellular matrices for scalable expansion of human ES/iPS cells. *Biomaterials*. **2017**, *124*, 47-54. DOI:10.1016/j.biomaterials.2017.01.039.

(44) Tang, Y.; Liu, L.; Li, J.; Yu, L.; Severino, F. P. U.; Wang, L.; Shi, J.; Tu, X.; Torre, V.; Chen, Y. Effective motor neuron differentiation of hiPSCs on a patch made of crosslinked monolayer gelatin nanofibers. *J. Mater. Chem. B.* **2016**, *4*, 3305-3312. DOI:10.1039/c6tb00351f.

(45) Tang, Y.; Liu, L.; Li, J.; Yu, L.; Wang, L.; Shi, J.; Chen, Y. Induction and differentiation of human induced pluripotent stem cells into functional cardiomyocytes on a compartmented monolayer of gelatin nanofibers. *Nanoscale*. **2016**, *8*, 14530-14540. DOI:10.1039/c6nr04545f.

(46) Li, X.; Liu, L.; Wang, L.; Kamei, K.-i.; Yuan, Q.; Zhang, F.; Shi, J.; Kusumi, A.; Xie, M.; Zhao, Z.; Chen, Y. Integrated and diffusion-based micro-injectors for open access cell assays. *Lab Chip.* **2011**, *11*, 2612-2617. DOI: 10.1039/c1lc20258h.

(47) Wang, L.; Zhang, Z.-L.; Wdzieczak-Bakala, J.; Pang, D.-W.; Liu, J.; Chen, Y. Patterning cells and shear flow conditions: convenient observation of endothelial cell remoulding, enhanced production of angiogenesis factors and drug response. *Lab Chip*. **2011**, *11*, 4235. DOI: 10.1039/c1lc20722a.

(48) Tang, Y.; Shi, J.; Li, S.; Wang, L.; Cayre, Y. E.; Chen, Y. Microfluidic device with integrated microfilter of conical-shaped holes for high efficiency and high purity capture of circulating tumor cells. *Sci. Rep.* **2014**, *4*, 6052. DOI:10.1038/srep06052.

(49) Kamei, K.-I.; Koyama, Y.; Tokunaga, Y.; Mashimo, Y.; Yoshioka, M.; Fockenberg, C.; Mosbergen, R.; Korn, O.; Wells, C.; Chen, Y. Characterization of Phenotypic and Transcriptional Differences in Human Pluripotent Stem Cells under 2D and 3D Culture Conditions. *Adv. Healthc. Mater*. **2016**, *5*, 2951-2958. DOI:10.1002/adhm.201600893.

(50) Chen, C.; He, Y.; Lopez, E.; Carreiras, F.; Yamada, A.; Schanne-Klein, M.-C.; Lambert, A.; Chen, Y.; Aimé, C. High-throughput tuning of ovarian cancer spheroids for on-chip invasion assays. *Micro and Nano Engineering*. **2022**, *15*, 100138. DOI:10.1016/j.mne.2022.100138.

(51) Dems, D.; Rodrigues Da Silva, J.; Helary, C.; Wien, F.; Marchand, M.; Debons, N.; Muller, L.; Chen, Y.; Schanne-Klein, M.-C.; Laberty-Robert, C.; Krins, N.; Aimé, C. Native Collagen: Electrospinning of Pure, Cross-Linker-Free, Self-Supported Membrane. *ACS Applied Bio Materials*. **2020**, *3*, 2948-2957. DOI:10.1021/acsabm.0c00006.

(52) Lopez Marquez, A.; Gareis, I. E.; Dias, F. J.; Gerhard, C.; Lezcano, M. F. Methods to Characterize Electrospun Scaffold Morphology: A Critical Review. *Polymers*. **2022**, *14*, 467. DOI:10.3390/polym14030467.

(53) Chen, X.; Nadiarynkh, O.; Plotnikov, S.; Campagnola, P. J. Second harmonic generation microscopy for quantitative analysis of collagen fibrillar structure. *Nat. Protoc.* **2012**, *7*, 654-669. DOI:10.1038/nprot.2012.009.

(54) Kurland, N. E.; Drira, Z.; Yadavalli, V. K. Measurement of nanomechanical properties of biomolecules using atomic force microscopy. *Micron*. **2012**, *43*, 116-128. DOI:10.1016/j.micron.2011.07.017.

(55) Rianna, C.; Kumar, P.; Radmacher, M. The role of the microenvironment in the biophysics of cancer. *Semin. Cell Dev. Biol.* **2018**, *73*, 107-114. DOI:doi: 10.1016/j.semcdb.2017.07.022.

(56) Alcaraz, J.; Otero, J.; Jorba, I.; Navajas, D. Bidirectional mechanobiology between cells and their local extracellular matrix probed by atomic force microscopy. *Semin. Cell Dev. Biol.* **2018**, *73*, 71-81. DOI:10.1016/j.semcdb.2017.07.020.

(57) Shi, Y.; Cai, M. J.; Zhou, L. L.; Wang, H. D. The structure and function of cell membranes studied by atomic force microscopy. *Semin. Cell Dev. Biol.* **2018**, *73*, 31-44. DOI:10.1016/j.semcdb.2017.07.012.

(58) Bitler, A.; Dover, R. S.; Shai, Y. Fractal properties of cell surface structures: A view from AFM. *Semin. Cell Dev. Biol.* **2018**, *73*, 64-70. DOI:10.1016/j.semcdb.2017.07.034.

(59) Viji Babu, P. K.; Rianna, C.; Mirastschijski, U.; Radmacher, M. Nano-mechanical mapping of interdependent cell and ECM mechanics by AFM force spectroscopy. *Sci. Rep.* **2019**, *9*, 12317. DOI:10.1038/s41598-019-48566-7.

(60) Liu, F.; Mih, J. D.; Shea, B. S.; Kho, A. T.; Sharif, A. S.; Tager, A. M.; Tschumperlin, D. J. Feedback amplification of fibrosis through matrix stiffening and COX-2 suppression. *J. Cell Biol.* **2010**, *190*, 693-706. DOI:10.1083/jcb.201004082.

(61) Brown, A. C.; Fiore, V. F.; Sulchek, T. A.; Barker, T. H. Physical and chemical microenvironmental cues orthogonally control the degree and duration of fibrosis-associated epithelial-to-mesenchymal transitions. *J Pathol*. **2013**, *229*, 25-35. DOI:10.1002/path.4114.

(62) Jorba, I.; Uriarte, J. J.; Campillo, N.; Farre, R.; Navajas, D. Probing Micromechanical Properties of the Extracellular Matrix of Soft Tissues by Atomic Force Microscopy. *J. Cell. Physiol.* **2017**, *232*, 19-26. DOI:10.1002/jcp.25420.

(63) Leggett, S. E.; Yun Sim, J.; Rubins, J. E.; Neronha, Z. J.; Kendall Williams, E.; Wong, I. Y. Morphological single cell profiling of the epithelial-mesenchymal transition. *Integr Biol (Camb).* **2016**, *8*, 1133-1144. DOI:10.1039/c6ib00139d.

(64) Postma, M.; Goedhart, J. PlotsOfData-A web app for visualizing data together with their summaries. *PLoS Biol.* **2019**, *17*, e3000202. DOI:10.1371/journal.pbio.3000202.

(65) Pastushenko, I.; Blanpain, C. EMT Transition States during Tumor Progression and Metastasis. *Trends Cell Biol.* **2019**, *29*, 212-226. DOI: 10.1016/j.tcb.2018.12.001.

(66) Beaufort, C. M.; Helmijr, J. C. A.; Piskorz, A. M.; Hoogstraat, M.; Ruigrok-Ritstier, K.; Besselink, N.; Murtaza, M.; van IJcken, W. F. J.; Heine, A. A. J.; Smid, M.; Koudijs, M. J.; Brenton, J. D.; Berns, E.M.J.J.; Helleman, J. Ovarian cancer cell line panel (OCCP): clinical importance of in vitro morphological subtypes. *PLoS One*. **2014**, *9*, e103988. DOI:10.1371/journal.pone.0103988.

(67) McGrail, D. J.; Kieu, Q. M. N.; Dawson, M. R. The malignancy of metastatic ovarian cancer cells is increased on soft matrices through a mechanosensitive Rho-ROCK pathway. *J Cell Sci.* **2014**, *127*, 2621-2626. DOI:10.1242/jcs.144378.

(68) Fan, Y.; Sun, Q.; Li, X.; Feng, J.; Ao, Z.; Li, X.; Wang, J. Substrate Stiffness Modulates the Growth, Phenotype, and Chemoresistance of Ovarian Cancer Cells. *Front Cell Dev Biol.* **2021**, *9*, 718834. DOI:10.3389/fcell.2021.718834.

(69) McKenzie, A. J.; Hicks, S. R.; Svec, K. V.; Naughton, H.; Edmunds, Z. L.; Howe, A. K. The mechanical microenvironment regulates ovarian cancer cell morphology, migration, and spheroid disaggregation. *Sci Rep.* **2018**, *8*, 7228. DOI: 10.1038/s41598-018-25589-0.

(70) Pieuchot, L.; Marteau, J.; Guignandon, A.; Dos Santos, T.; Brigaud, I.; Chauvy, P.-F.; Cloatre, T.; Ponche, A.; Petithory, T.; Rougerie, P.; Vassaux, M.; Milan, J.-L.; Wakhloo, N.T.; Spangenberg, A.; Bigerelle, A.; Anselme, K. Curvotaxis directs cell migration through cell-scale curvature landscapes. *Nature Commun.* **2018**, *9*, 3995. DOI:10.1038/s41467-018-06494-6.

For Table of Contents Use Only

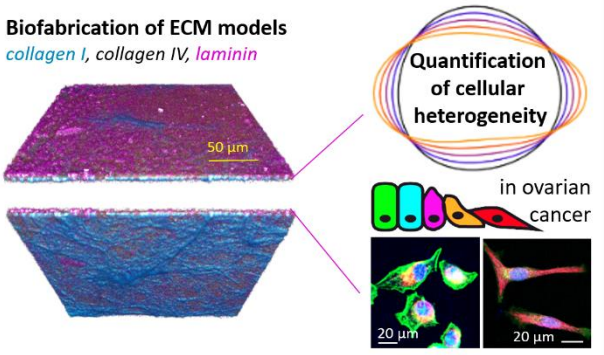

3D collagen topology shapes cell morphology, beyond stiffness

Changchong Chen,§ Zeinab Ibrahim,§ Marion F. Marchand,± Tristan Piolot,± Sahil Kamboj,# Franck Carreiras,# Ayako Yamada,§ Marie-Claire Schanne-Klein,¦ Yong Chen,§ Ambroise Lambert# and Carole Aimé*§*